



This is the accepted manuscript made available via CHORUS. The article has been published as:

Strong-field nonsequential double photoionization using virtual-detector theory with path summation

Daniel Younis and Joseph H. Eberly

Phys. Rev. A **107**, 053117 — Published 30 May 2023

DOI: [10.1103/PhysRevA.107.053117](https://doi.org/10.1103/PhysRevA.107.053117)

Strong-field nonsequential double photoionization using virtual detector theory with path summation

Daniel Younis* and Joseph H. Eberly

Center for Coherence and Quantum Optics, and Department of Physics and Astronomy,
University of Rochester, Rochester, New York 14627, USA

(Dated: March 8, 2023 (submitted), May 4, 2023 (revised))

We present an *ab initio* study of the nonsequential strong-field ionization dynamics of a model two-electron atom with helium character. Single- and double-ionization events are characterized and displayed using detector signals extracted at different points in the two-electron two-dimensional space. The double photoelectron momentum distribution is calculated via coherent path-summation over virtual particle trajectories. A comparison is made between the momentum distributions obtained by the virtual detector method, the Schrödinger wavefunction, and the time-dependent surface flux method developed by Tao and Scrinzi [New J. Phys. **14**, 013021 (2012)]. Insights into different ionization and electron recollision pathways are gained from detailed virtual-particle tracking and energy-time readouts. This study demonstrates the extension of virtual detector theory to strong-field multi-electron quantum dynamics and highlights the importance of the evolving quantum phase in quasi-classical electron propagation.

I. INTRODUCTION

Ionization is the necessary precursor to many strong-field phenomena, including above-threshold ionization [1–7], nonsequential multiple ionization [8–10], high-harmonic generation [11–14], and laser-induced electron rescattering [15, 16]. Many aspects of the single-active-electron ionization process are accessible theoretically on the basis of radiative perturbation theory and the strong-field approximation, or the Keldysh-Faisal-Reiss theory [17–19] (see [20] for a recent review). In this approach, the scattered electron + field system is treated as a Volkov state [21] and the effect of the atomic potential is included perturbatively.

Nonsequential multiple ionization [7] is characterized by strong inter-electron correlations that can promote cooperative electron exit dynamics [8–10]. It is predominantly initiated when a first electron tunnels through the field-suppressed coulombic barrier and, in the next field half-cycle, is accelerated and field-driven back toward the nucleus. Exchange of momentum with the residual bound electrons increases the likelihood of excitation or tunnel ionization thereafter. The result is an anomalous ionization yield that can greatly exceed what is predicted by the sequential theory [22].

Due to the possibility of such inter-electron correlations, *ab initio* numerical methods are indispensable in laser-atom interaction studies involving field intensities near to or greater than the atomic unit $I \simeq 10^{16}$ W/cm². For a two-electron model atom, direct numerical integration of the time-dependent Schrödinger equation (TDSE) in full dimensions is the most accurate approach, but it is computationally expensive beyond 3 wavefunction degrees of freedom [23, 24] because the number of grid points in the discretely-sampled volume grows exponentially with each added dimension. The development of

ad hoc models to treat the two-electron wavefunction in reduced dimensionality is ongoing. For instance, in Ref. [25] a 3D coordinate system is introduced which accounts for inter-electron correlations in full dimensionality while restricting the center-of-mass motion to the field polarization axis. Attractive alternate schemes to TDSE integration include the quantum trajectory method [26, 27] which represents the wavefunction as a collection of fluid elements obeying the Madelung-Bohm quantum hydrodynamic equations [28, 29], and the classical ensemble method [30–32] which considers a large collection of particles whose initial conditions and statistical properties are determined by the initial wavefunction. Classical and semi-classical models are particularly useful for performing trajectory analysis of specific features that appear in the correlated photoelectron momentum distribution [33].

More recently, a hybrid quantum-classical approach known as the virtual detector method was initiated by Feuerstein and Thumm [34], which has been extended to include virtual particles [35, 36] and their quantum phase information [37]. In the virtual particle calculation, one introduces an enclosure of purely numerical “detectors”

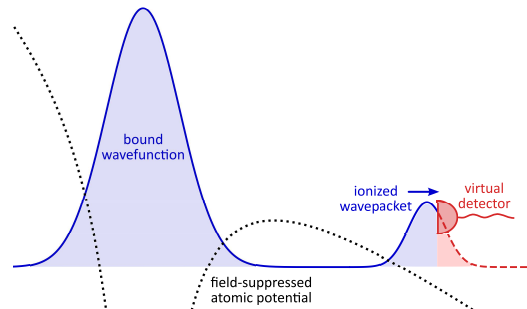


FIG. 1. Illustration of the numerical detection process, in which a “virtual detector” extracts information from incident wavepackets.

* dan.younis@outlook.com

around the region where the TDSE is integrated. The exterior of the enclosure is relatively far from the ionization inception, and the result of each detection can be interpreted as the creation of a virtual particle with calculated momentum and phase that carries information about the quantum state, see Fig. 1. The motion of the virtual particle is then described classically. In this way, the accuracy of the fully quantum-mechanical solution on a grid close to the atomic nucleus can be combined with the efficiency of classical propagation beyond the enclosure, where additional quantum effects are negligible.

The use of the virtual detector method has proven successful in a variety of ways. Originally, it was developed to extract photoelectron momentum data from outward-bound wavepackets at the computation domain boundary, similarly to the time-dependent surface flux method (*t*-SURFF) [38–40] which will be discussed in more detail in Sec. III C (Results). However, the virtual detectors can be placed at any region of interest, and have in the past been employed to extract key information close to the atomic nucleus as well. For example, in analyzing an ionization event independent of a tunneling assumption, the virtual detector method allows one to obtain centrally important features of ionization including those associated with the popular tunneling picture, such as the tunneling entrance and exit positions and the electron’s effective tunneling rate (see cautions by Ivanov, *et al.* [41], and [42, 43]). The strong-field recollision scenario relies on determinations of such quantities, which virtual detectors have been able, sometimes uniquely, to provide.

In this article, we extend the theory based on virtual detection to two-electron atomic systems. The generalization to three or more interacting electrons readily follows from our reformulation of virtual detector theory. For concreteness, we demonstrate the calculation for a model helium atom and its nonsequential ionization dynamics under strong-field irradiation. We employ the aligned-electron approximation [44–46] wherein the motion of each electron is constrained to the field polarization axis. Thus, our two-dimensional system consists of 2 one-dimensional electrons identified by their positions (x_1, x_2) and momenta (p_1, p_2) on two such independent polarization-aligned coordinates. A comparison will be made between the photoelectron momentum distributions calculated using the virtual detector method, the Schrödinger wavefunction, and the *t*-SURFF method. Accordingly, the TDSE integration volume in our calculation will be larger than the virtual detector boundary in order to retain the ionized wavefunction components for benchmarking.

The rest of this article is organized as follows. In Section II, we review the numerical methods relevant to the calculation and discuss the two-electron extension of virtual detector theory. In Section III, we present and analyze calculation results of the evolving wavefunction, virtual detector signals, photoelectron momentum distributions, and virtual-particle trajectories. In Section

IV, we summarize and conclude this work. Atomic units (a.u.) are employed except where indicated otherwise.

II. METHOD

The virtual detector method is a hybrid quantum-classical approach. As such, the first step is to numerically integrate the time-dependent Schrödinger equation $i\partial\Psi/\partial t = H\Psi$ on a discrete space-time mesh. In our case, this is accomplished using the Peaceman-Rachford alternating-direction implicit method [47, 48] which interleaves Crank-Nicolson propagation in the two spatial dimensions:

$$\begin{aligned}\Psi(t + \frac{\delta t}{2}) &\leftarrow (1 + \frac{i\delta t}{2}H_2)^{-1}(1 - \frac{i\delta t}{2}H_1)\Psi(t) \\ \Psi(t + \delta t) &\leftarrow (1 + \frac{i\delta t}{2}H_1)^{-1}(1 - \frac{i\delta t}{2}H_2)\Psi(t + \frac{\delta t}{2})\end{aligned}\quad (1)$$

where $H_n \equiv -\frac{1}{2}[\partial^2/\partial x_n^2 - V(\vec{x}, t)]$ are sub-Hamiltonians with $V(\vec{x}, t)$ the total potential energy. This scheme (1) propagates the wavefunction forth one time-step interval δt with a single-step error of $\mathcal{O}(\delta t^3)$. It must be noted that it violates unitarity depending on the degree of non-commutativity between H_1 and H_2 . For the Hamiltonian considered in this work (given below), we have verified that $[H_1, H_2] \approx 0$ to within numerical error and therefore unitarity is preserved well.

As the wavefunction $\Psi(\vec{x}, t)$ evolves, virtual detectors densely arranged along the enclosure net intercept it and perform non-destructive numerical detections at their respective positions \vec{x}_d for every calculation time-step t_d . The features extracted in the detection are the local phase, probability current, and momentum:

$$\phi_0 = \arctan(\text{Im } \Psi / \text{Re } \Psi)|_{(\vec{x}_d, t_d)} \quad (2)$$

$$\vec{j}_0 = \frac{i}{2}(\Psi \nabla \Psi^* - \Psi^* \nabla \Psi)|_{(\vec{x}_d, t_d)} \quad (3)$$

$$\vec{p}_0 = \nabla \phi \equiv \vec{j}_0 / \rho|_{(\vec{x}_d, t_d)} \quad (4)$$

where $\rho = |\Psi|^2$ is the two-electron probability density. Since the detectors generally lie between numerical grid points, $\Psi(\vec{x}, t)$ must be interpolated to each point \vec{x}_d in these expressions.

Equations (2)–(4) initiate a virtual particle at the space-time point of detection (\vec{x}_d, t_d) with initial momentum \vec{p}_0 and a statistical weight w equal to the probability density ρ at birth. Its subsequent motion is governed by Hamilton’s classical equations ($d\vec{x}/dt = \partial H / \partial \vec{p}$, $d\vec{p}/dt = -\partial H / \partial \vec{x}$) which we integrate numerically using the 4th-order Runge-Kutta method. Thus, the representation of outward-bound wavepackets is converted from a quantum wave to a classical particle density description, and likewise the Hamiltonian changes from a quantum operator to a classical function as the interpretation switches. The evolution of one virtual particle in (x_1, x_2) -space represents the dynamical behavior of two classical electrons, and its trajectory signifies a possible two-electron ionization pathway from the ensemble of cases.

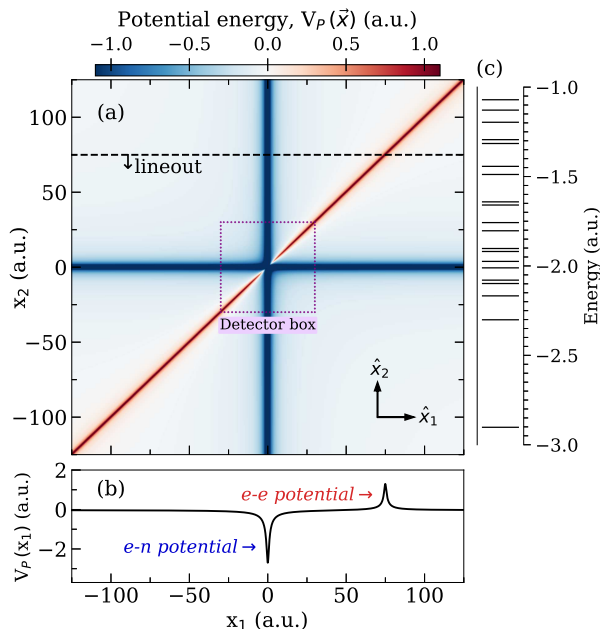


FIG. 2. (Color online). (a) Potential energy map of the model two-electron atom with the virtual detector box overlaid. One-dimensional interaction potentials are obtained from lineouts parallel to the coordinate axes \hat{x}_1/\hat{x}_2 as in panel (b). The 20 lowest eigenenergies of this model atom’s spectrum are displayed in panel (c).

Under irradiation by high-intensity, low-frequency, and/or long-duration pulses, the spatial domain may not be able to accommodate the Schrödinger wavefunction far from the nucleus. Thus, at the domain boundary one typically employs a masking function or negative complex potential [49] to numerically absorb ionized wavefunction components. In contrast, the virtual-particle description of the wavefunction is not restricted to a grid. Moreover, virtual particles do not interact (but the two electrons they represent interact pairwise), so their time-evolution also offers the advantage of computation in parallel.

The Hamiltonian

$$H(\vec{x}, \vec{p}, t) = \sum_{n=1}^2 \left[\frac{1}{2} p_n^2 - Z_0 V(x_n) \right] + V(x_1 - x_2) + (x_1 + x_2)E(t) \quad (5)$$

consists of electron-nuclear (e - n) and electron-electron (e - e) screened coulombic potentials of the form $V(x) = 1/\sqrt{x^2 + \sigma^2}$ in addition to a length-gauge field interaction term under the dipole approximation [44, 45]. Here, Z_0 is the nuclear charge, $E(t)$ is the laser electric field, and σ is a screening parameter. The non-zero value for σ controls the $1/x$ coulombic singularity in $V(x)$, and it also determines the model atomic spectrum and ionization energy. It must be noted that the model potential in Eq. (5) does not give a correct second ionization threshold, such that the sequential double-ionization yield is unreasonably large. This discrepancy is important for

comparing numerical calculations with experimental results [50, 51] (see Sec. III C).

A. Calculation parameters

We take $Z_0 = +2$ and $\sigma = 0.74$ a.u. for a ground-state energy of -2.902 a.u. (≈ -79 eV) corresponding closely to that of helium. Figure 2(a) illustrates the spatial dependence of the total atomic potential energy and includes the detector box. It has a side-length of 60 a.u. and consists of 500 detectors distributed uniformly along its perimeter. The separation between neighboring detectors is chosen to be finer than the spatial resolution of the discrete wavefunction, making the enclosure effectively complete in the sense that probability current density does not pass the detector box unregistered. Figure 2(b) is a lineout for fixed x_2 which illustrates the potential experienced by an electron when the other is 75 a.u. away from the nucleus. Lastly, Fig. 2(c) shows part of the eigenenergy spectrum of this model atom.

The wavelength of the field is 780 nm (frequency $\omega = 0.0584$ a.u.) and its peak intensity is 0.5 PW/cm² (amplitude $E_0 = 0.119$ a.u.). These parameters correspond to the so-called nonsequential double ionization “knee” regime in helium, where the e - e correlation strength is enhanced [22, 52]. We take the temporal profile of the laser pulse amplitude to be trapezoidal with a 6-cycle plateau period and a 2-cycle linear turn-on and turn-off, equaling a total pulse duration of 26 fs (the duration of one optical cycle (o.c.) is $2\pi/\omega = 2.6$ fs).

III. RESULTS

A. Wavefunction dynamics

In this coordinate representation, the two-electron wavefunction is attracted to the x_1 and x_2 axes by the nuclear potential, and it is repelled away from the $x_1 = x_2$ diagonal due to inter-electron repulsion (see Fig. 2). With every half-cycle, the field tilts the total potential experienced by both electrons, energetically raising or lowering it toward either the positive or negative side of their axes. The four quadrants of the position-space are readily understood: population in the $x_1 x_2 > 0$ regions signifies a non-zero probability of detecting both electrons on the same side of the nucleus, and conversely for population in the $x_1 x_2 < 0$ regions. Additionally, near-axis population far from the origin indicates that one electron is bound while the other is well ionized.

A time-sequence of the $2e$ probability density $\rho(\vec{x}, t)$ is shown in Fig. 3. Here, one observes the formation of double-ionization (DI) jets every half-cycle, corresponding to the ejection of both electrons in the same direction $x_1 x_2 > 0$. Alternatively, probability density develops in

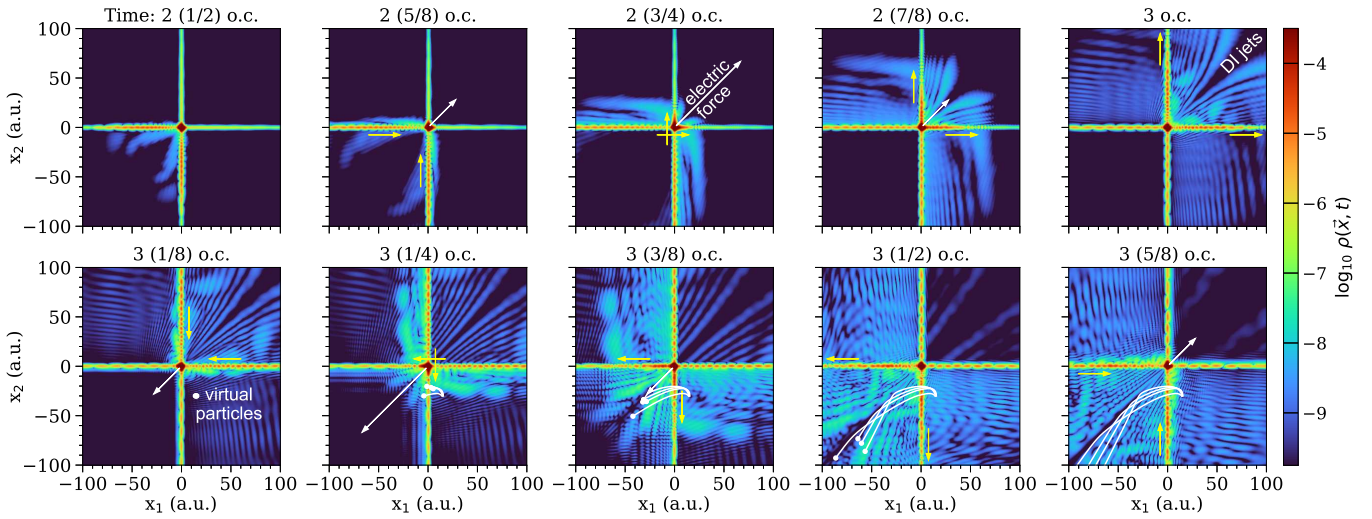


FIG. 3. (Color online). Snapshots of the two-electron probability density $\log_{10} \rho(\vec{x}, t)$. White arrow: instantaneous laser electric force vector, $-(\hat{x}_1 + \hat{x}_2)E(t)$. Yellow arrows: direction of probability current flow on-axis. The trajectories of four virtual particles initiated at 3 (1/8) o.c. are shown, which subsequently follow the stream of probability current.

the $x_1 x_2 < 0$ quadrants primarily due to sequential field-ionization, i.e., the electrons tunneling in opposite directions during opposite field half-cycles. The subsequent dynamics can be understood from the trajectory evolution of virtual particles. Consider the four particles born at $t_d = 3$ (1/8) o.c. around $\vec{x}_d = (15, -30)$ a.u. as shown in Fig. 3, all of which represent sequentially-ionized electron pairs. As the field reverses direction, the trajectories illustrate how the first electron is driven back toward the origin after which it scatters off the nuclear potential and contributes to the double-ionizing jet population. This reveals that double-ionization jets are not formed solely because of both electrons tunneling out in the same laser half-cycle. It is important to note how the virtual particles closely mimic the wavefunction probability density despite evolving according to a classical equation of motion.

B. Virtual detector signals

The virtual detector signals also provide insight into the ionization process, particularly regarding the timing of events. In Fig. 4(a), the readouts of axial probability current $j_1(t) = \vec{j}(t) \cdot \hat{x}_1$ from the left- and right-most detectors at $\vec{x}_d = (\pm 30, 0)$ a.u. are provided. With each laser half-cycle, a probability current signal of comparable duration is registered which lags the field crest by $\sim 1/4$ th of a cycle. These axial, inward-directed current signals are of particular relevance to the recollision scenario of strong-field ionization, for they are associated with the virtual particles of bound-recolliding electron pairs (their dynamical behavior will be analyzed in what follows). In Fig. 4(b), the two components of $\vec{j}(t)$ are provided for the detector at $\vec{x}_d = (30, 14)$ a.u., which ac-

cording to Fig. 3 is in the path of a double-ionization jet. In this case, the probability current signal lags the electric field crest by $\sim 1/8$ th of a cycle.

The $j_n(t)$ signals provided in Figs. 4(a) and 4(b) represent single- and double-ionization events, respectively, due to their associated detection points in space. Comparing the signal amplitudes, it is seen that the current density for single ionization is approximately two orders of magnitude stronger than that for double ionization. Lastly, the sub-cycle oscillations in $j_n(t)$ are due to spatiotemporal wavefunction interference, and the signals are modulated by the laser pulse profile in addition to the depletion of bound population over time.

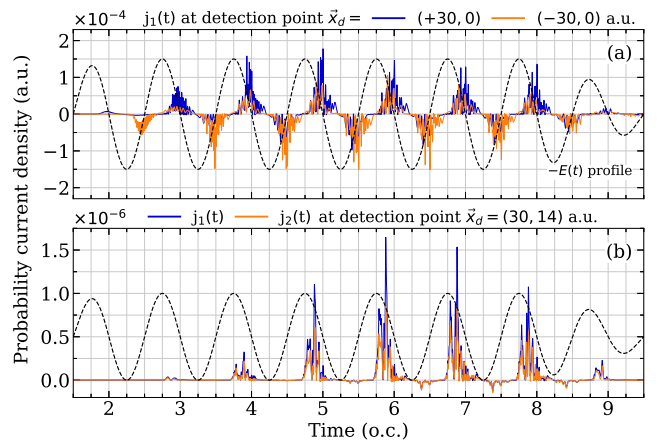


FIG. 4. (a) Time series of the \hat{x}_1 -directed probability current density measured 30 a.u. to the right/left (in blue/orange) of the atomic core. (b) Time series of the \hat{x}_1/\hat{x}_2 components of $\vec{j}(t)$ (in blue/orange) measured at the detection point $(30, 14)$ a.u. Dashed line: laser electric force profile.

C. Photoelectron momentum distribution

The 2- e probability density exhibits a complex spatial interference structure arising from field-driven collisions between different wavepacket components (as evidenced in Fig. 3). The virtual detector method captures this information by associating to each particle an initial phase, given by the local wavefunction phase at birth, and tracking its evolution [37]. This brings the quantum-classical correspondence between the wavefunction and virtual-particle descriptions closer.

The phase calculation is based on the observation that the quantum wave of a virtual particle may be approximated by a Volkov state [20, 21]:

$$\Psi_{v,\vec{k}}(\vec{x}, t) = (2\pi)^{-1} \exp(i\vec{k} \cdot \vec{x}) \exp[-iS(t)] \quad (6)$$

where \vec{k} is the wavevector and $S(t) = \int dt L$ is the action integral of Lagrangian L . In accordance with $\Psi_{v,\vec{k}}(\vec{x}, t)$, the evolving virtual-particle phase is

$$\phi(t) = \phi_0 - \vec{p}(t) \cdot \vec{x}(t) + S(t) \quad (7)$$

where ϕ_0 is the initial phase from Eq. (2) and $\vec{p}(t)$ is the instantaneous virtual-particle momentum. At the end of the pulse, the photoelectron momentum distribution (PMD) is calculated by binning the virtual-particle weights with their path-integrated phase terms from Eq. (7):

$$W(\vec{p}) = \left| \sum_{n=1}^N \sqrt{w_n} \exp(i\phi_n) \right|^2 \text{ for } \vec{p}_n \in [\vec{p}, \vec{p} + \delta\vec{p}] \quad (8)$$

where N is the total number of virtual particles and $\delta\vec{p}$ is the vector of momentum bin widths. Virtual particles for which either electron is still bound to the nucleus are omitted from the summation to produce the distribution of doubly-ionized electron pairs.

From the final position-space wavefunction $\Psi(\vec{x})$, the photoelectron momentum distribution can also be calculated via Fourier transformation after applying a suitable masking function $\mathcal{M}(\vec{x})$ to filter the bound population:

$$\Phi(\vec{p}) = \frac{1}{2\pi} \int d^2x e^{-i\vec{p} \cdot \vec{x}} (\mathcal{M}\Psi)(\vec{x}). \quad (9)$$

In this case, $\mathcal{M}(\vec{x})$ is a cross-shaped Gaussian filter that smoothly attenuates the bound population and all singly-ionized wavepackets within 50 a.u. of the axes. Further, a cross-shaped momentum-space filter was applied to $\Phi(\vec{p})$ to remove population for which either photoelectron momentum was low.

A third and related method of calculating the PMD is the time-dependent surface flux (t -SURFF) method [38–40]. Briefly, it is based on time-integrating the wavefunction as it passes through a surface in the far field, analogously to the virtual detector box in Fig. 2. However, in this case the ionized wavepackets are projected onto

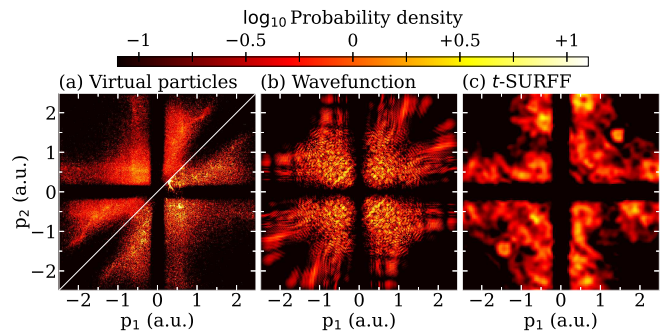


FIG. 5. The double photoelectron momentum distribution calculated using (a) 54 million virtual electron pairs in $W(\vec{p})$, (b) the free-space wavefunction $\Phi(\vec{p})$, and (c) the time-dependent surface-flux amplitude $\mathcal{F}(\vec{p})$. The upper half of panel (a) illustrates the effect of neglecting the virtual-particle phase.

Volkov states whose momenta correspond to the observation values of interest. Under the aligned 2- e model geometry considered here, the t -SURFF momentum probability amplitude is given by [40]

$$\mathcal{F}(\vec{p}) = \iint R_i dt d\varphi \times \left[\hat{r} \cdot \Psi_{v,\vec{p}}^*(\vec{x}, t) [\vec{A}(t) - \frac{i}{2}(\nabla + i\vec{p})] \Psi(\vec{x}, t) \right] \Big|_{|\vec{x}|=R_i} \quad (10)$$

wherein $\vec{A}(t)$ is the vector potential whose two components are equal to $-\int dt' E(t')$, R_i is the surface integration radius, and $\hat{r} = (\cos \varphi, \sin \varphi)$ for $\varphi = \arctan(x_2/x_1)$.

In Fig. 5, the double photoelectron momentum distributions calculated using $W(\vec{p})$, $\Phi(\vec{p})$, and $\mathcal{F}(\vec{p})$ are provided. In panel (a), the phase-included half of $W(\vec{p})$ (lower diagonal) is sharper than its phase-omitted counterpart (upper diagonal), and it reveals more of the speckled interference pattern exhibited also by $\Phi(\vec{p})$. This calculation demonstrates one of the key applications of the virtual detector method; it is able to effectively encode ionized wavepacket information in the form of virtual particles and accurately reproduce the far-field PMD that would be obtained by full wavefunction analysis. Furthermore, it is advantageous for analyzing specific features in the PMD via trajectory back-propagation. The virtual-particle distribution is also in excellent qualitative agreement with that obtained by the classical ensemble method in a similar intensity and wavelength regime (cf. Fig. 3 in Ref. [53]). However, the resolution is much finer in this case due to the greater number of electron pairs that comprise the distribution, which is on the order of 10^7 , versus the 10^5 members used in Ref. [53].

The t -SURFF PMD in Fig. 5(c) was calculated using 10^3 surface points at $R_i = 90$ a.u. in Eq. (10), and the integration time-step was 0.1 a.u. which corresponds to approximately 10^3 evaluations per field cycle. In this case, we find that the t -SURFF PMD lacks many of the fine details contained in the virtual-particle and Schrödinger

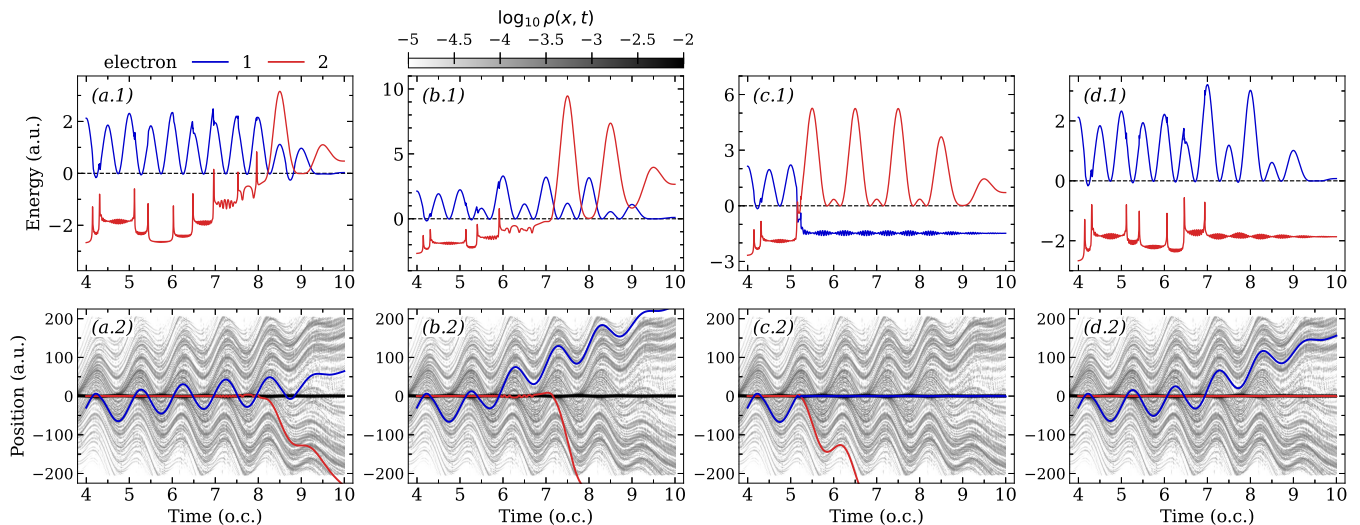


FIG. 6. (Color online). (a.1)–(d.1) Energy-time evolution and (a.2)–(d.2) position-time evolution of representative virtual electron pairs. The latter set is overlaid on the 1D-projected evolving wavefunction probability density $\log_{10} \rho(x, t)$ shown in grayscale. Initially, electron 1 (in blue) is ionized, while electron 2 (in red) is bound. Inter-electron collisions appear as sharp cusps in energy, most prominently seen in the bound electron curves. The four sets of panels show (a) nonsequential double ionization, (b) recollision-excitation with subsequent ionization, (c) bound-ionized electron swapping, and (d) failure to double-ionize after multiple collisions.

wavefunction PMDs, but qualitatively they share a similar overall structure. This may be due in part to a failure in the Volkov approximation when the two electrons interact strongly. Additionally, we have found that when the t -SURFF and virtual detector parameters are set equal (equating the t -SURFF integration radius and the detector box size, number of surface points and number of detectors, and so on) the t -SURFF PMD does not accurately approximate $\Phi(\vec{p})$. This suggests that the virtual detector method can operate on generally smaller TDSE integration volumes than the t -SURFF method.

In calculations involving single-active-electron atoms, interference rings appear in the PMDs whose radii are integer multiples of $\sqrt{2}\omega$ [37]. Thus, they correspond energetically to local maxima in the above-threshold ionization spectrum. In the two-electron case, the e - e interaction further complicates the energy transfer mechanisms in the atom-field system, and the ripple-like pattern in Fig. 5 does not have a direct interpretation. Furthermore, the maximum cutoffs in the PMDs correspond approximately to $E_0/\omega \approx 2$ a.u., which is the momentum amplitude of a classical electron oscillating in a plane electromagnetic wave.

To conclude this section, we remark on the similarities and differences between the PMDs calculated in this work and those obtained experimentally in Refs. [50, 51], which employ the cold target recoil ion momentum spectroscopy (COLTRIMS) [54, 55] coincidence technique. First of all, the characteristic ‘V’ shape in the $p_1 p_2 > 0$ quadrants is accurately reproduced by our numerical calculations as in experiment, and the momentum magnitudes are also in good agreement. The field intensity and wavelength

considered here are both closest to that in Ref. [50], but both experimental studies suggest a comparatively larger probability of measuring electron pairs with longitudinal momenta $p_1 \approx p_2$. This discrepancy may be due to the model screened coulomb potential used in Eq. (5), whose incorrect second-ionization threshold leads to an exaggerated sequential double-ionization yield, as noted previously. This results in a greater fraction of the population occupying the anti-correlated $p_1 p_2 < 0$ quadrants of the PMD. Moreover, as discussed in Ref. [46], the coulombic repulsion in the aligned-electron model (characterized by the diagonal band in the potential of Fig. 2) is exaggerated and so tends to distort the double-ionization data as it prevents the electrons from being ejected in the same direction with similar momenta. Attempts have been made to resolve this deficiency in the aligned-electron approximation, such as the Eckhardt-Sacha model [56] which leads to more accurate ionization yield and momentum distribution data [57–59].

D. Virtual electron trajectories

Recall that a single virtual particle in this calculation represents an interacting pair of virtual electrons. A key advantage of the virtual detector method is that their dynamical variables can be tracked in time, providing a classical view into the ionization and e - e interaction processes that is similar to the classical ensemble method and is reminiscent of alternate formulations of Schrödinger theory such as Bohmian mechanics [29] and the Feynman path-integral approach [60].

TABLE I. The range of initial energies and momenta of the virtual electron pairs shown in Fig. 6.

Electron no.	1 (in blue)	2 (in red)
Energy	2.13 ± 10^{-2} a.u.	-2.67 ± 10^{-2} a.u.
Momentum	2.07 ± 10^{-2} a.u.	$(-4.3 \pm 0.2) \times 10^{-2}$ a.u.

In this calculation, there are ~ 50 million virtual particles, equal to the product of the total number of detectors and discrete time-steps used. Figure 6(a.1)–(d.1) (top row) shows the energy-time evolution of a few representative virtual electron pairs which undergo multiple collision events. In Fig. 6(a.2)–(d.2) (bottom row), their corresponding position-time trajectories are shown overlaid on the one-dimensional projection of the evolving wavefunction probability density $\rho(x, t) = |\int dx' \Psi(x, x', t)|^2$ which in this case is symmetric between electrons $x \leftrightarrow x'$. Note once more how the virtual electron trajectories accurately mimic the wavefunction's oscillatory behavior.

Each virtual electron pair considered here was initialized at $(x_1, x_2) = (-30, 0)$ a.u. a few time-steps apart, beginning around the 4th field cycle. According to Fig. 4(a) (orange curve), the probability current at this position and time is flowing in the positive direction toward the nucleus, which signals an upcoming bound-free e - e collision. In all cases, the first electron is ionized while the second electron is still bound. In Table I, the range of initial energies and momenta of each virtual electron pair is provided to convey their proximity. However, their subsequent dynamical behavior is significantly different, as evidenced in Fig. 6, revealing the high degree of sensitivity of the interaction on the initial conditions which are derived from the wavefunction. For instance, Fig. 6(a) illustrates the process of nonsequential double ionization (NSDI) [22, 31, 52] in which a series of energetically favorable collisions occurring approximately every half-cycle causes the bound electron to transition into the continuum. Figure 6(b) shows the related process of recollision-excitation with subsequent ionization (RESI) [61] in which, following a collision event, the bound electron occupies an excited intermediate state (in this case, between $t \approx 6-7$ o.c.) from which it is later field-ionized.

Figure 6(c) illustrates a situation in which the bound and ionized electrons swap following interaction, resulting in a singly-ionized atomic state. In this case, the first electron is recaptured by the nucleus after thrice-colliding with the second electron, which emerges in the continuum with more than double the initial energy of the former. Lastly, Fig. 6(d) shows multiple e - e collision events that ultimately fail to liberate the bound electron. This suggests that double ionization is more sensitive to the timing of energy transfers, between the electrons themselves and the electrons with the field, than it is to the overall number of collision events. Evidently, the diverse range of correlated inter-electron behavior can be interpreted in a direct way using the virtual detector method.

IV. CONCLUSION

We have demonstrated how the virtual detector method can be applied to probe the evolution of a two-electron atom and its nonsequential ionization dynamics arising from strong-field irradiation. The detector signals and virtual particle dynamical variables provide valuable insights into the behaviors leading up to single- and double-ionization events, and the electron trajectories accurately mimic the wavefunction evolution in space and time. Furthermore, the virtual particle momentum distribution including path-integrated phase information agrees qualitatively with the full quantum-mechanical solution based on numerical integration of the time-dependent Schrödinger equation. Thus, one can use the virtual detector method to accurately produce the momentum distribution that would be obtained by full wavefunction analysis on a comparatively large integration volume. The possibility of applying the virtual detector method to elucidate other ionization-related processes may be explored in the near future.

ACKNOWLEDGMENTS

The work reported here was supported by the grant DE-FG02-05ER15713 funded by the U.S. Department of Energy, Office of Science. Calculations were performed on the BlueHive supercomputing cluster at the University of Rochester.

-
- [1] J. H. Eberly and P. Lambropoulos, eds., *Multiphoton Processes* (Wiley, New York, 1978).
 - [2] N. B. Delone and V. P. Krainov, *Atoms in Strong Light Fields* (Springer-Verlag, Berlin, 1985).
 - [3] S. J. Smith and P. L. Knight, eds., *Multiphoton Processes* (Cambridge Univ. Press, Cambridge, 1988).
 - [4] M. V. Fedorov, *Atomic and Free Electrons in a Strong Light Field* (World Scientific Publishing, Singapore, 1997).
 - [5] P. Agostini, F. Fabre, G. Mainfray, G. Petite, and N. K. Rahman, *Phys. Rev. Lett.* **42**, 1127 (1979).
 - [6] J. H. Eberly, J. Javanainen, and K. Rzażewski, *Physics Reports* **204**, 331 (1991).
 - [7] P. B. Corkum, *Phys. Rev. Lett.* **71**, 1994 (1993).
 - [8] A. Becker, R. Dörner, and R. Moshhammer, *J. Phys. B: At. Mol. Opt. Phys.* **38**, S753 (2005).
 - [9] W. Becker and H. Rottke, *Contemp. Phys.* **49**, 199 (2008).
 - [10] W. Becker, X. J. Liu, P. J. Ho, and J. H. Eberly, *Rev. Mod. Phys.* **84**, 1011 (2012).
 - [11] A. L'Huillier, K. J. Schafer, and K. C. Kulander, *J. Phys. B: At. Mol. Opt. Phys.* **24**, 3315 (1991).

- [12] M. Lewenstein, Ph. Balcou, M. Yu. Ivanov, A. L’Huillier, and P. B. Corkum, *Phys. Rev. A* **49**, 2117 (1994).
- [13] F. Krausz and M. Ivanov, *Rev. Mod. Phys.* **81**, 163 (2009).
- [14] M. Chini, K. Zhao, and Z. Chang, *Nat. Photon.* **8**, 178 (2014).
- [15] P. Corkum, *Phys. Today* **64**, 36 (2011).
- [16] F. Schell, T. Bredtmann, C. P. Schulz, S. Patchkovskii, M. J. J. Vrakking, and J. Mikosch, *Sci. Adv.* **4**, eaap8148 (2018).
- [17] L. V. Keldysh, *Zh. Eksp. Teor. Fiz.* **47**, 1945 (1964); *Sov. Phys. JETP* **20**, 1307 (1965), (English translation).
- [18] F. H. M. Faisal, *J. Phys. B: At. Mol. Opt. Phys.* **6**, 553 (1973).
- [19] H. R. Reiss, *Phys. Rev. A* **22**, 770 (1980).
- [20] S. V. Popruzhenko, *J. Phys. B: At. Mol. Opt. Phys.* **47**, 204001 (2014).
- [21] D. M. Wolkow, *Z. Physik* **94**, 250 (1935).
- [22] B. Walker, B. Sheehy, L. F. DiMauro, P. Agostini, K. J. Schafer, and K. C. Kulander, *Phys. Rev. Lett.* **73**, 1227 (1994).
- [23] E. S. Smyth, J. S. Parker, and K. T. Taylor, *Comput. Phys. Commun.* **114**, 1 (1998).
- [24] J. S. Parker, B. J. S. Doherty, K. T. Taylor, K. D. Schultz, C. I. Blaga, and L. F. DiMauro, *Phys. Rev. Lett.* **96**, 133001 (2006).
- [25] C. Ruiz, L. Plaja, L. Roso, and A. Becker, *Phys. Rev. Lett.* **96**, 053001 (2006).
- [26] C. L. Lopreore and R. E. Wyatt, *Phys. Rev. Lett.* **82**, 5190 (1999).
- [27] R. E. Wyatt and C. J. Trahan, *Quantum Dynamics with Trajectories* (Springer, New York, 2006).
- [28] E. Madelung, *Z. Physik* **40**, 322 (1927).
- [29] D. Bohm, *Phys. Rev.* **85**, 166 (1952); *Phys. Rev.* **85**, 180 (1952).
- [30] R. Panfili, J. H. Eberly, and S. L. Haan, *Opt. Express* **8**, 431 (2001).
- [31] P. J. Ho, R. Panfili, S. L. Haan, and J. H. Eberly, *Phys. Rev. Lett.* **94**, 093002 (2005).
- [32] P. J. Ho and J. H. Eberly, *Phys. Rev. Lett.* **95**, 193002 (2005).
- [33] D. F. Ye, X. Liu, and J. Liu, *Phys. Rev. Lett.* **101**, 233003 (2008).
- [34] B. Feuerstein and U. Thumm, *J. Phys. B: At. Mol. Opt. Phys.* **36**, 707 (2003).
- [35] X. Wang, J. Tian, and J. H. Eberly, *Phys. Rev. Lett.* **110**, 243001 (2013).
- [36] X. Wang, J. Tian, and J. H. Eberly, *J. Phys. B: At. Mol. Opt. Phys.* **51**, 084002 (2018).
- [37] R.-H. Xu and X. Wang, *AIP Advances* **11**, 025124 (2021).
- [38] L. Tao and A. Scrinzi, *New J. Phys.* **14**, 013021 (2012).
- [39] A. Scrinzi, *New J. Phys.* **14**, 085008 (2012).
- [40] V. Mosert and D. Bauer, *Computer Physics Communications* **207**, 452 (2016).
- [41] M. Y. Ivanov, M. Spanner, and O. Smirnova, *J. Mod. Opt.* **52**, 165 (2005).
- [42] N. Teeny, E. Yakaboylu, H. Bauke, and C. H. Keitel, *Phys. Rev. Lett.* **116**, 063003 (2016).
- [43] J. Tian, X. Wang, and J. H. Eberly, *Phys. Rev. Lett.* **118**, 213201 (2017).
- [44] J. Javanainen, J. H. Eberly, and Q. Su, *Phys. Rev. A* **38**, 3430 (1988).
- [45] S. L. Haan, P. S. Wheeler, R. Panfili, and J. H. Eberly, *Phys. Rev. A* **66**, 061402(R) (2002).
- [46] D. K. Efimov, A. Maksymov, J. S. Prauzner-Bechcicki, J. H. Thiede, B. Eckhardt, A. Chacón, M. Lewenstein, and J. Zakrzewski, *Phys. Rev. A* **98**, 013405 (2018).
- [47] D. Bauer, ed., *Computational Strong-Field Quantum Dynamics* (De Gruyter, Berlin, 2017).
- [48] D. W. Peaceman and H. H. Rachford, Jr., *J. Soc. Indust. Appl. Math.* **3**, 28 (1955).
- [49] J.-Y. Ge and J. Z. H. Zhang, *J. Chem. Phys.* **108**, 1429 (1998).
- [50] A. Staudte, C. Ruiz, M. Schöffler, S. Schössler, D. Zeidler, T. Weber, M. Meckel, D. M. Villeneuve, P. B. Corkum, A. Becker, and R. Dörner, *Phys. Rev. Lett.* **99**, 263002 (2007).
- [51] A. Rudenko, V. L. B. de Jesus, T. Ergler, K. Zrost, B. Feuerstein, C. D. Schröter, R. Moshhammer, and J. Ullrich, *Phys. Rev. Lett.* **99**, 263003 (2007).
- [52] W.-C. Liu, J. H. Eberly, S. L. Haan, and R. Grobe, *Phys. Rev. Lett.* **83**, 520 (1999).
- [53] P. J. Ho, *Phys. Rev. A* **72**, 045401 (2005).
- [54] R. Dörner, V. Mergel, O. Jagutzki, L. Spielberger, J. Ullrich, R. Moshhammer, and H. Schmidt-Böcking, *Phys. Rep.* **330**, 95 (2000).
- [55] J. Ullrich, R. Moshhammer, A. Dorn, R. Dörner, L. Ph. H. Schmidt, and H. Schmidt-Böcking, *Rep. Prog. Phys.* **66**, 1463 (2003).
- [56] K. Sacha and B. Eckhardt, *Phys. Rev. A* **63**, 043414 (2001).
- [57] J. S. Prauzner-Bechcicki, K. Sacha, B. Eckhardt, and J. Zakrzewski, *Phys. Rev. Lett.* **98**, 203002 (2007).
- [58] J. S. Prauzner-Bechcicki, K. Sacha, B. Eckhardt, and J. Zakrzewski, *Phys. Rev. A* **78**, 013419 (2008).
- [59] B. Eckhardt, J. S. Prauzner-Bechcicki, K. Sacha, and J. Zakrzewski, *Chemical Physics* **370**, 168 (2010).
- [60] R. P. Feynman and A. R. Hibbs, *Quantum Mechanics and Path Integrals* (McGraw-Hill, New York, 1965).
- [61] X. Hao, Y. Bai, C. Li, J. Zhang, W. Li, W. Yang, M. Liu, and J. Chen, *Commun. Phys.* **5**, 31 (2022).